FISEVIER

Contents lists available at ScienceDirect

Scripta Materialia

journal homepage: www.elsevier.com



Effects of Au²⁺ irradiation induced damage in a high-entropy pyrochlore oxide single crystal

Candice Kinsler-Fedon ^{a, *}, Lauren Nuckols ^a, Christopher Nelson ^b, Zehui Qi ^c, Qing Huang ^d, David Mandrus ^{a, e}, Yanwen Zhang ^{a, e}, William J. Weber ^a, Veerle Keppens ^{a, *}

- ^a Department of Materials Science and Engineering, University of Tennessee, Knoxville, TN 37996, USA
- ^b The Center for Nanophase Materials Sciences, Oak Ridge National Laboratory, Oak Ridge, TN 37831
- ^c Department of Nuclear Engineering, University of Tennessee, Knoxville, Tennessee 37996, USA
- d Department of Physics and Astronomy, University of Tennessee, Knoxville, Tennessee 37996, USA
- e Materials Science and Technology Division, Oak Ridge National Laboratory, Oak Ridge, Tennessee 37831, USA

ARTICLE INFO

Article history: Received 17 March 2022 Received in revised form 13 June 2022 Accepted 5 July 2022

Keywords:
High-entropy pyrochlore
Ion irradiation
Single crystal
Rutherford backscattering spectrometry
Transmission electron microscopy

ABSTRACT

We report an ion-irradiation study of a compositionally complex (high-entropy) pyrochlore oxide. The damage produced from 4 MeV Au²⁺ ion irradiation on single crystal (Yb_{0.2}Tm_{0.2}Lu_{0.2}Ho_{0.2}Er_{0.2})₂Ti₂O₇ aligned along the [100] direction is investigated at room temperature by Rutherford backscattering spectrometry in channeling mode (RBS/C). Damage profiles based on RBS/C are presented and compared to single-component pyrochlore titanate oxides to evaluate the relative resistance to irradiation-induced amorphization. The results show that this high-entropy pyrochlore goes amorphous at a dose of 0.13 dpa, which is comparable to that of single-component pyrochlores previously studied. Transmission electron microscopy images unveil the damaged surface layer, which is consistent with the RBS/C results.

© 20XX

Rare-earth (RE) pyrochlore oxides (RE₂B₂O₇) possess a multitude of unique properties, including exotic magnetism [1-2], low thermal conductivity [3-4], resistance against radiation amorphization [5-6], and enhanced ionic conductivity [7]. The flexibility and phase stability of the cubic pyrochlore structure allows for a multitude of compositions that can be tuned to express desired properties or new functionalities, such as increased electrical or ionic conductivity and structure/phase transformations that enhance mechanical and chemical durability [8-9]. When considering materials for nuclear waste management, the RE23+Ti24+O7 pyrochlore materials have been studied extensively by the incorporation of actinides [5-12]. Rare-earth titanate pyrochlores respond to ion irradiation by transforming to an amorphous state once a specific local damage dose is reached under given irradiation conditions [5]. The specific dose for the amorphous transition is highly dependent upon the incident ion mass and energy, as well as the size of the rare-earth cation. Until now, no studies have been reported on the

 $\label{eq:https://doi.org/10.1016/j.scriptamat.2022.114916} $1359\text{-}6462\@\@20XX$$

effects of irradiation-induced damage on a high-entropy titanate pyrochlore single-crystal to understand its amorphization behavior.

High-entropy oxides (HEOs), also referred to as configurationally complex oxides (CCOs), refer to oxides with multiple ions (five or more) on a single site [13-14]. Extending the study of ternary rare-earth pyrochlore oxides and their radiation response to the area of HEOs and multicomponent materials is necessary to improve or expand our options for storing nuclear waste and radioactive materials. At the same time, controlled response to ion irradiation offers potential for tuning properties and creating new functionalities in these compounds. Because multicomponent materials typically possess heavily distorted lattices and improved chemical durability, these materials can be highly attractive for radiation applications [15]. Within the past few years, radiation damage related research has gained momentum for configurationally complex materials, such as high-entropy alloys (HEAs) [15–18], high-entropy carbides [19–20], and even more recently highentropy oxides that have been proposed as nuclear waste forms [21-23]. Some novel findings from these recent reports include improved radiation resistance for alloys and carbides, enhanced mechanical properties at elevated temperatures, excellent structural stabilities, and high corrosion resistance. However, the radiation response of HEOs is not yet known. The tunability of the chemical and mechanical prop-

^{*} Corresponding author.

*E-mail addresses: ckinsle1@vols.utk.edu (C. Kinsler-Fedon),
vkeppens@utk.edu (V. Keppens).

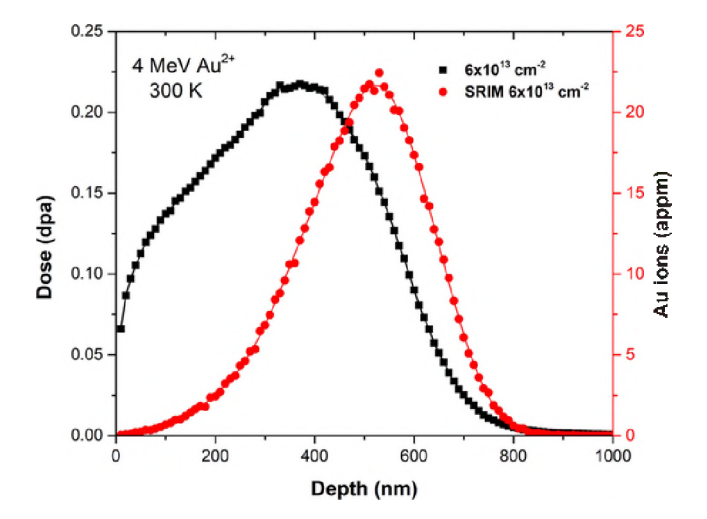


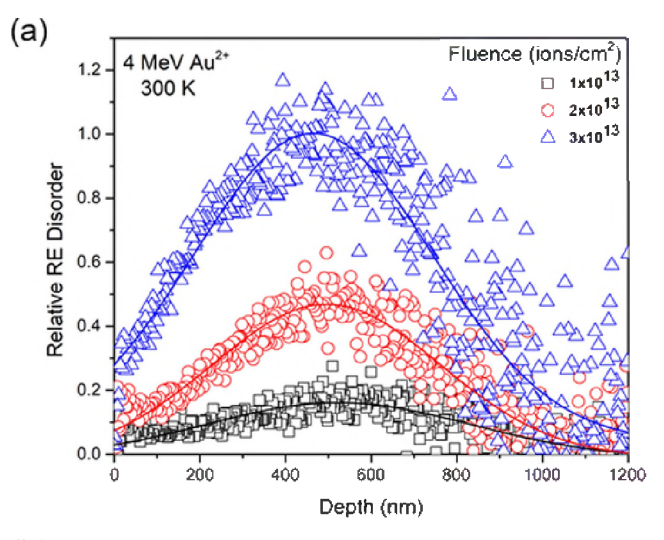
Fig. 1. The depth profiles of local damage dose (dpa), represented by solid black squares, and implanted Au concentration (appm), represented by solid red circles predicted by SRIM simulations for an ion fluence of 6×10^{13} cm⁻². Solid lines are fits to the data (color online).

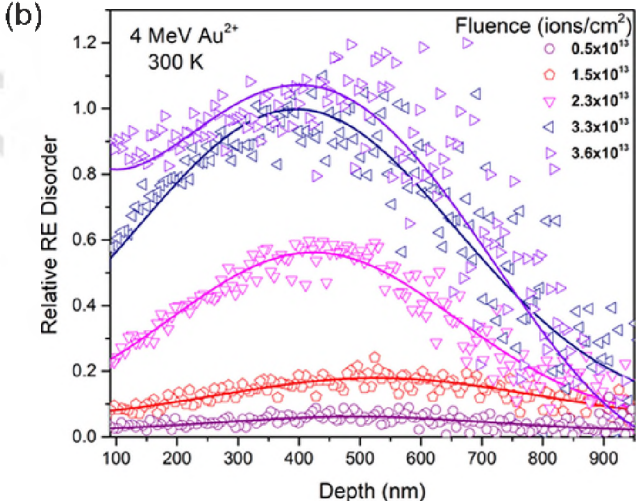
erties by manipulating the number of cations, the entropy site disorder, and mixing possibilities can enhance the properties and lead to a wider range of possible applications.

Because irradiation damage in single-component pyrochlore oxides has been studied in detail [24–27], an examination of irradiation effects in a high-entropy pyrochlore oxide is a logical extension. Large, high-quality single crystals of $(Yb_{0.2}Tm_{0.2}Lu_{0.2}Ho_{0.2}Er_{0.2})_2Ti_2O_7$ have been grown via the floating zone technique, making it an ideal candidate for quantitative analysis of radiation damage accumulation profiles by Rutherford backscattering spectrometry in channeling mode (RBS/C). The unique availability of a high-entropy single crystal pyrochlore allows direct comparison of RBS/C damage accumulation profiles to those for single-component RE pyrochlores.

The single crystal $(Yb_{0.2}Tm_{0.2}Lu_{0.2}Ho_{0.2}Er_{0.2})_2Ti_2O_7$ was grown using the floating-zone growth technique and a two-mirror optical floating-zone furnace (Canon Machinery model SC1-MDH) with 1500-W halogen lamps. This crystal growth procedure is similar to that describing the growth of another high-entropy titanate pyrochlore [28], using oxygen atmosphere at a pressure of 0.2 MPa and a growth rate of 5–6 mm per hour. Laue diffraction, using a Huber X-ray diffractometer and HD-CR 35 NDT, was employed to determine crystal quality and align the crystal along the [100] direction for ion beam bombardment, as illustrated in Fig. S2. An oval-shaped piece, roughly 9 mm in length and 1 mm in thickness, was cut from the oriented rod and polished to a mirror finish.

Room temperature Au-ion irradiations and ion beam analysis via RBS/C were performed using the 3 MeV tandem accelerator and associated facilities at the Ion Beam Materials Laboratory at the University of Tennessee, Knoxville [29]. 4 MeV Au²⁺ ions were employed to ensure damage is shallow enough to be measured using RBS/C analysis. It also allows for direct comparison of the disordering behavior to singlecomponent RE pyrochlores [27-31]. Irradiations were performed 4° off the normal surface to limit channeling effects in the single crystal. Ion fluences ranged from 5 \times 10¹² to 6 \times 10¹³ cm⁻² to induce a range of damage states in the target material. A flux of $4.2 \times 10^{11} \text{ cm}^{-2}\text{s}^{-1}$ was constant for all the irradiations. The irradiating beam was slightly wobbled and defocused so that the resulting damage was uniform. Two areas of the sample surface were each irradiated to 3 different fluences (6 total), with RBS/C measurements conducted after each fluence. After this irradiation sequence, the sample was repolished, and two areas were again irradiated to 3 different fluences (6 total), with RBS/C spectra collected after each fluence.





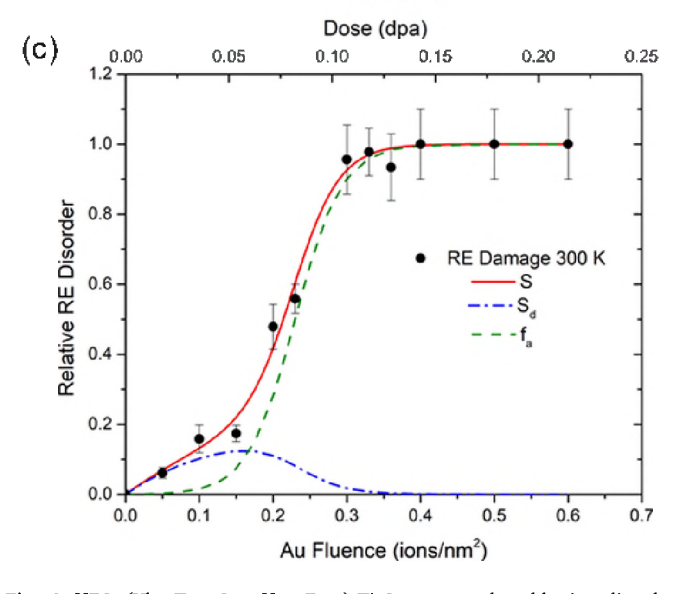


Fig. 2. HEO $(Yb_{0.2}Tm_{0.2}Lu_{0.2}Ho_{0.2}Er_{0.2})_2Ti_2O_7$ rare-earth sublattice disorder curves following 4 MeV Au²⁺ irradiation with ion fluences ranging from (a) 1 to 3 (\times 10¹³ cm⁻²) and (b) 0.5 to 3.6 (\times 10¹³ cm⁻²). The solid lines represent fits to the data. (c) Relative rare-earth disorder at the damage peak as a function of Au fluence and dose. The solid red line is the fit of the damage accumu-

■ lation along with the amorphous region f_a (dashed line) and the residual crystalline region S_d (dashed/dotted line) (color online).

In-situ damage accumulation along the [100] direction was determined using RBS/C under high ($< 2.0 \times 10^{-7}$ torr) vacuum using a 3.5 MeV He $^+$ ion beam to obtain quantitative RBS/C spectra to a depth of ~850 nm. Disorder profiles were determined from the RBS/C spectra using the iterative procedure described elsewhere [32]. The Stopping and Range in Matter code (SRIM code) [33], in full-cascade mode [34], was used to determine the depth profiles of atomic displacements for the 4 MeV Au ions. The threshold displacement energies for all the ions in the target material were set to 50 eV [35] and an experimentally derived density of 7 g/cm³ was used in the SRIM simulations.

TEM was performed using a FEI Titan at 300 kV on specimens prepared from the two final irradiated areas corresponding to fluences of 3.33×10^{13} and 3.66×10^{13} cm $^{-2}$. Diffraction contrast images were captured using the two-beam condition with the sample tilted slightly off the zone axis to isolate diffraction from the (001) normal planes. The specifications for TEM preparation of the crystal sample are described in the Supplemental Material.

Based on the SRIM simulations, the depth profiles of local damage dose (displacements per atom or dpa) and implanted Au concentration at the highest ion fluence in this study (6 \times $10^{13}~\rm cm^{-2})$ are shown in Fig. 1. The predicted damage profiles for all ion fluences employed in this irradiation experiment are provided in Fig. S6 in the supplemental material. Under these irradiation conditions, the damage peak is at a depth of \sim 400 nm, and the peak concentration of implanted Au is predicted to be at \sim 520 nm.

Two separate irradiation experiments under identical conditions were performed on the same single crystal sample, which was repolished to remove damage from the first irradiation experiment prior to the second irradiation. The disorder accumulation curves shown in Figs. 2a and 2b represent the two separate experiments and show the depth profiles of damage accumulation at various ion fluences, from 0.5 to 3.6×10^{13} cm⁻², on the RE sublattice. To obtain these damage profiles, an iterative process [32] using the raw RBS spectra (Fig. S5 in supplemental material) has been performed to generate the disorder in the material versus depth. This process allows for the removal of dechanneling effects and is commonly employed for this purpose [30–32].

Using the experimentally derived density of 7 g/cm 3 for the SRIM simulations, the He ion stopping power as a function of energy was determined for the HEO pyrochlore, and the energy difference per channel was used to determine the depth. Ultimately, these depth profiles show that the disorder increases with increasing ion fluence and a slight shift of the damage peak toward the surface, resulting in a fully amorphous material at the damage peak for a fluence of about 3.66 \times 10^{13} cm $^{-2}$.

The accumulation of relative rare-earth disorder at the damage peak as a function of ion fluence and local damage dose is shown in Fig. 2(c). In order to describe this damage accumulation behavior, a disorder accumulation model is employed [27–31]. Eq. (1) represents this model, with S being the total irradiation-induced disorder, f_a is the amorphous fraction, and S_d is the defect-induced disorder in the remaining damaged crystalline regions.

$$S = f_a + S_d \tag{1}$$

This model is also referred to as the DI/DS model (direct-impact, defect-stimulated) [36]. For the amorphous fraction, Eq. (2) describes the relationship between σ_a (direct amorphous cross section), σ_s (defect-stimulated amorphous cross section), and D is either the local dose (in dpa) or ion fluence.

$$f_a = 1 - \left(\sigma_a + \sigma_s\right) / \left\{\sigma_s + \sigma_a \exp\left(\sigma_a + \sigma_s\right) D\right\}$$
 (2)

To account for the damage caused by defects in the crystalline structure, Eq. (3) quantitatively represents this damage given the saturation value S_d^* and a constant B that corresponds to the cross section relating to the probability of defect recombination processes [27].

$$S_d = S_d^* \left[1 - \exp(-BD) \right] \left(1 - f_a \right) \tag{3}$$

Fig. 2(c) summarizes the collective results from this damage accumulation model, showing the contributions from f_a and S_d and a fit to the mixed RE disorder at the damage peak at ambient temperature. The relative RE disorder as a function of Au fluence (ions/nm²) and dose (dpa) reveals a nonlinear behavior with complete amorphization shown at ~ 0.13 dpa and 4 MeV Au fluences of ~ 0.37 (ions/nm²). These results are comparable to similar studies on other rare-earth titanate pyrochlores [27–31], and Table 1 summarizes the ion fluence and dose experimentally found for attaining complete amorphization at the damage peak in each composition. The HEO pyrochlore's dose for amorphization appears to be slightly higher than ${\rm Ho_2Ti_2O_7}$, indicating more radiation resistance, but lower than that for ${\rm Sm_2Ti_2O_7}$, suggesting less radiation resistance. Likewise, when compared to ${\rm Gd_2Ti_2O_7}$, which was irradiated under similar conditions (4 MeV Au ions), the HEO pyrochlore appears to be less radiation resistant.

It must also be noted that the Au ion energies are lower for $\rm Sm_2Ti_2O_7$ and $\rm Ho_2Ti_2O_7$ (1 MeV), which may affect a direct comparison with the HEO pyrochlore (4 MeV). Under 1 MeV Kr ion irradiation, the critical dose for amorphization of simple rare-earth titanate pyrochlores at room temperature varies by up to a factor of three depending on the specific rare-earth element on the A-site [6]; however, the critical dose under 0.6 MeV Bi ion irradiation is 0.18 \pm 0.01 dpa for $\rm A_2Ti_2O_7$ (A = Y, Sm, Gd, Lu) pyrochlores [35], which is comparable to the results in Table 1. The HEO pyrochlore in this study may represent the behavior of a mixture of pyrochlores with a range of critical doses (amorphization resistance), but additional studies on relevant rare-earth pyrochlores under identical heavy-ion irradiation conditions are needed to better understand this behavior.

The amorphization parameters derived from the model fit discussed above are listed in Table 2, along with those experimentally found for $\mathrm{Gd}_2\mathrm{Ti}_2\mathrm{O}_7$ from a previous study [27]. Because σ_s is significantly larger than σ_a , defect-stimulated amorphization is the primary mechanism for overall amorphization in this HEO. At low doses up to \sim 0.065 dpa, the disorder caused by defects, S_d , has a greater influence on the HEO. At doses greater than \sim 0.07 dpa, the defect-stimulated increase of the amorphous fraction, f_a , becomes dominant. These phenomena are similar to previous reports for the typical, single-component titanate pyrochlores; however, this effect occurs at a higher dose in the HEO com-

Table. 1

Comparison of the HEO pyrochlore irradiation conditions and fluence/dose for achieving amorphous state at damage peak with those of single-component rare-earth titanate pyrochlores.

Rare-Earth Titanate Pyrochlore Composition	Irradiation Species	Ion Fluence for Amorphization	Amorphization Dose (dpa)	Reference
Gd ₂ Ti ₂ O ₇	4.0 MeV Au	$4.5 \times 10^{13} \mathrm{cm}^{-2}$	0.15	[27]
$\mathrm{Sm_2Ti_2O_7}$	1.0 MeV Au	$4.0 \times 10^{13} \mathrm{cm}^{-2}$	0.14	[30]
$\mathrm{Ho_{2}Ti_{2}O_{7}}$	1.0 MeV Au	$2.7 \times 10^{13} \mathrm{cm}^{-2}$	0.12	[31]
$(Yb_{0.2}Tm_{0.2}Lu_{0.2}Ho_{0.2}Er_{0.2})_2Ti_2O_7$	4.0 MeV Au	$3.6 \times 10^{13} \mathrm{cm}^{-2}$	0.13	

Table. 2 Comparison of the HEO's amorphization model parameters to $Gd_2Ti_2O_7$ [27]. These parameters were determined from data fits shown in Figs. 2(c) and 3.

Amorp	hization Parameters	HEO RE sublattice	Gd sublattice
σ_{a}	$0.022\mathrm{nm}^2$	$0.50 \pm 0.25 \mathrm{nm}^2$	
$\sigma_{\mathbf{s}}$	$31.65\mathrm{nm}^2$	$13 \pm 2 \mathrm{nm}^2$	
S_d^*	$0.3\mathrm{nm}^2$	$0.15 \pm 0.4 \mathrm{nm}^2$	
В	$5~\mathrm{nm}^2$	$2.8 \pm 4 \mathrm{nm}^2$	

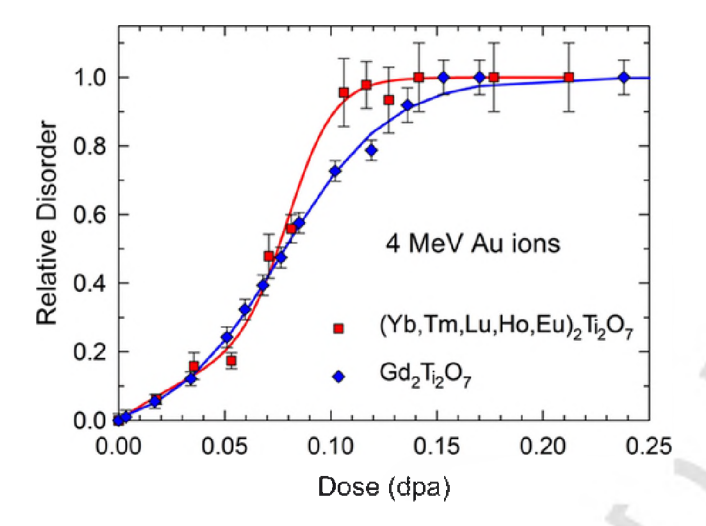


Fig. 3. Comparison of rare-earth disorder at the damage peak as a function of dose between reported $Gd_2Ti_2O_7$ [27] and HEO $(Yb_{0.2}Tm_{0.2}Lu_{0.2}Ho_{0.2}Er_{0.2})_2Ti_2O_7$ single crystals with 4.0 MeV Au ions at 300 K. The solid lines are fits to the damage data points (color online).

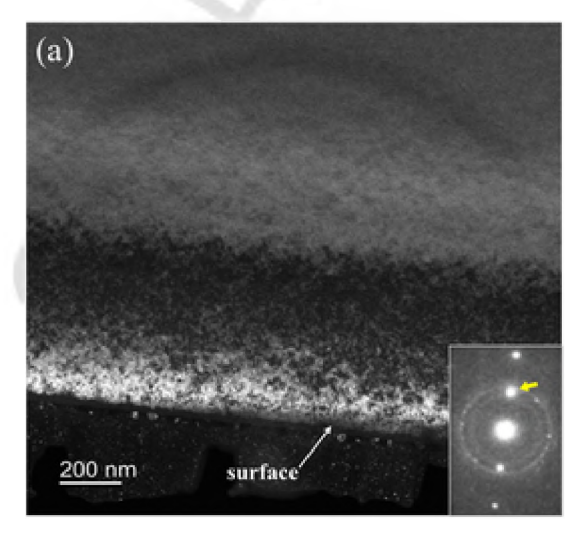
pared to the Ho and Sm pyrochlores (\sim 0.03 dpa) [30–31]. The accumulation of disorder at the damage peak for the HEO titanate pyrochlore and $Gd_2Ti_2O_7$ are compared in Fig. 3 for similar 4 MeV Au ion irradiations at room temperature. There are notable differences in disordering behavior between the two pyrochlores, as illustrated in Table 2 and Fig. 3. At lower doses, the behavior of the two pyrochlores is relatively similar, but at a dose of \sim 0.09 dpa, a clear divergence in the total irradiation-induced disorder is shown. This divergence indicates that $Gd_2Ti_2O_7$ has a slower rate of defect-stimulated amorphization compared to that of the HEO pyrochlore, which is also reflected by the

higher defect-stimulated cross section σ_s for the HEO found in Table 2. The HEO pyrochlore does have a smaller direct amorphization cross section σ_a meaning that it is slightly less susceptible to direct amorphous behavior upon impact of heavy ions. From these results, it can be concluded that $Gd_2Ti_2O_7$ has slightly higher radiation resistance than the HEO at room temperature.

Cross-sectional TEM was conducted to characterize the resulting radiation damage of the HEO pyrochlore single crystal. Figs. 4(a) and 4(b) are dark field micrographs showing the surface layer of damage at ion fluences of 3.33 and 3.66 ($\times~10^{13}~\rm cm^{-2}$), respectively. The highly-strained damaged region, clearly extends from the surface to ~ 800 nm in depth, with a peak in damage at a depth of 450 to 550 nm, which is consistent with the RBS/C results and SRIM predictions. Beyond this depth, a virgin region of crystal exists that is unaffected by the ion beam. High resolution images (Figs. S7(b) and S7(c)) reveal that the highly damaged regions consist of a mixture of amorphous and residual crystalline material. There are no discernable extended defects. This is consistent with cation interstitial defects and a disorder-stimulated amorphous transition as the primary factors leading to amorphization in this HEO crystal composition when exposed to 4 MeV Au irradiation, as predicted by the DI/DS model previously discussed.

The local atomic displacements on the A lattice sites due to the random distribution of rare-earth cations may contribute to an increased instability and susceptibility to amorphization. The dark-light mottled contrast in the damaged layer is evidence of damage appearing as strained residual crystalline regions (light contrast) and unstrained amorphous regions (dark contrast) in Figs. 4(a) and 4(b). An amorphous surface layer, roughly 20 nm thick, is observed (Fig. S7(b)) that transitions into a mixture of residual crystalline and amorphous material beyond 20 nm from the surface. While the SAED patterns indicate the presence of amorphous material, this may be due to amorphous material in the damaged layer and/or the amorphous graphite capping material. The TEM results are consistent with the RBS/C data fits in Fig. 2 (c) and in Table 2 that predict defect-stimulated amorphization is the primary cause of the observed crystalline to amorphous transition. While details of defect and structural evolution during amorphization are not fully known, they are the subject of an ongoing investigation.

In summary, a single crystal of the novel HEO pyrochlore $(Yb_{0.2}Tm_{0.2}Lu_{0.2}Ho_{0.2}Er_{0.2})_2Ti_2O_7$ was successfully synthesized, and its response to ion irradiation was quantified using RBS/C. 4 MeV Au²⁺irradiation was employed with ion fluences from 0.5 to 6 \times 10¹³ cm⁻² at ambient temperature. Under these conditions, a local amorphous state in the HEO occurs at an ion fluence of 3.66 \times 10¹³ cm⁻² and a damage



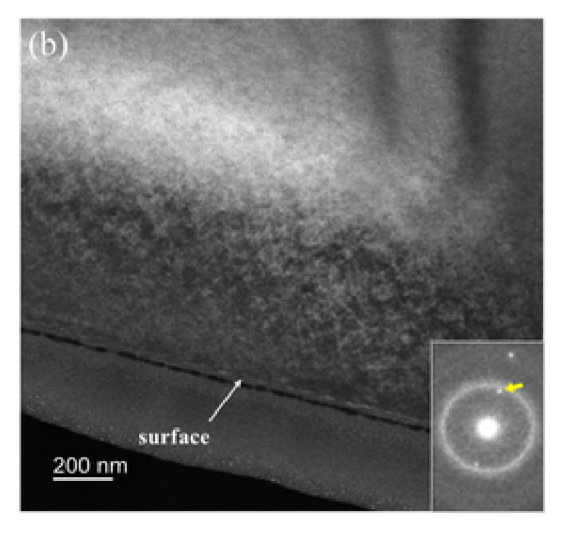


Fig. 4. Cross-sectional TEM dark-field micrographs unveiling the damaged regions near the surface of the irradiated HEO pyrochlore crystal with 4 MeV Au²⁺ ions corresponding to the regions irradiated to ion fluences of (a) 3.33×10^{13} cm⁻² and (b) 3.66×10^{13} cm⁻². Insets are SAED patterns taken on-axis, with the arrows highlighting the image forming g-vector (color online).

dose of ~0.13 dpa. From these results, it appears that the HEO may be slightly more resistant to amorphization than the single component Ho pyrochlore but less radiation resistant than the Sm and Gd pyrochlores. More studies are being conducted to gain a complete understanding of this HEO's amorphization resistance at various temperatures. Given the promise of advanced properties in multicomponent oxides, expanding the study to include a variety of compositions and different structures with various levels of ion complexity will contribute to a better understanding of their response to irradiation damage. In addition, it is possible that irradiation of configurationally complex pyrochlore oxides can increase ionic conductivity or enhance magnetic properties, as observed in other amorphous pyrochlores [11–38]. As the properties or functionalities of irradiation damaged HEOs are largely unknown, further studies are warranted.

Declaration of Competing Interest

The authors have no known financial or personal competing interests.

Acknowledgements

CKF acknowledges support from the Center for Materials Processing at the University of Tennessee and NSF Grant # DMR-1808964. DGM acknowledges support from the National Science Foundation, Grant # DMR-1808964. XRD was performed at the Institute for Advanced Materials and Manufacturing (IAMM) Diffraction Facility, located at The University of Tennessee, Knoxville. TEM and analysis by C.T.N. supported by the U.S. Department of Energy, Office of Science, Basic Energy Sciences, Materials Sciences and Engineering Division. The irradiations and RBS/C measurements were performed under partial support from the University of Tennessee Governor's Chair program and the National Science Foundation, Grant # DMR-1808964.

Supplementary materials

Supplementary material associated with this article can be found, in the online version, at doi:10.1016/j.scriptamat.2022.114916.

References

- [1] J.S. Gardner, M.J.P. Gingras, J.E. Greedan, Rev. Mod. Phys. 82 (2010) 53.
- [2] J.E. Greedan, J. Alloys Compd. (2006) 444–455, 408–412.
- [3] M. Zhao, X. Ren, J. Yang, W. Pan, J. Am. Ceram. Soc 99 (2016) 293–299.
- [4] P.K. Schelling, S.R. Phillpot, R.W. Grimes, Philos. Mag. Lett. 84 (2004) 127–137.
- [5] R.C. Ewing, W.J. Weber, J. Lian, J. Appl. Phys. 95 (2004) 5949.
- 6] J. Lian, J. Chen, L.M. Wang, R.C. Ewing, J.M. Farmer, L.A. Boatner, K.B. Helean, Phys. Rev. B. 68 (2003) 134107.
- [7] B.J. Wuensch, K.W. Eberman, C. Heremans, E.M. Ku, P. Onnerud, E.M.E. Yeo, S.M. Haile, J.K. Stalick, J.D. Jorgensen, Solid State Ionics 129 (2000) 111–133.
- [8] G.R. Lumpkin, R.D. Aughterson, Front. Chem 9 (2021) 778140.
- [9] R. Sachan, E. Zarkadoula, X. Ou, C. Trautmann, Y. Zhang, M.F. Chisholm,

- W.J. Weber, ACS Appl. Mater. Interfaces 10 (2018) 16731-16738.
- [10] W.J. Weber, A. Navrotsky, S. Stefanovsky, E.R. Vance, E. Vernaz, MRS Bull. 34 (2009) 46–53.
- [11] P.E. Raison, R.G. Haire, T. Sato, T. Ogawa, MRS Online Proc. Library 556 (1998) 3.
- [12] W.J. Weber, R.C. Ewing, MRS Online Proc. Library 713 (2001) 31.
- [13] C.M. Rost, E. Sachet, T. Borman, A. Moballegh, E. Dickey, D. Hou, J. Jones, S. Curtarolo, J.-.P. Maria, Nat. Commun. 6 (2015) 8485.
- [14] B.L. Musico, D. Gilbert, T.Z. Ward, K. Page, E. George, J. Yan, D. Mandrus, V. Keppens, APL Mater., 8 (2020) 040912.
- [15] E.J. Pickering, A.W. Carruthers, P.J. Barron, S.C. Middleburgh, D.E.J. Armstrong, A.S. Gandy, Entropy 23 (2021) 98.
- [16] T. Egami, M. Ojha, O. Khorgolkhuu, D.M. Nicholson, G.M. Stocks, JOM 67 (2015) 2345–2349.
- [17] S.-Q. Xia, Z. Wang, T.-F. Yang, Y. Zhang, J. Iron Steel Res. Int. 22 (2015) 879–884.
- [18] N.A.P. Kiran Kumar, C. Li, K.J. Leonard, H. Bei, S.J. Zinkle, Acta Mater 113 (2016) 230–244.
- [19] F. Wang, X. Yan, T. Wang, Y. Wu, L. Shao, M. Nastasi, Y. Lu, B. Cui, Acta Mater 195 (2020) 739–749.
- [20] Y. Zhu, J. Chai, Z. Wang, T. Shen, L. Niu, S. Li, P. Jin, H. Zhang, J. Li, M. Cui, J. Eur. Ceram. Soc. 42 (2022) 2567–2576.
- [21] H. Tisdale, M. Christian, G. Morrison, T. Besmann, K. Sun, G. Was, H.C. zur Loye, Chem. Mater., Article ASAP (2022), https://doi.org/10.1021/ acs.chemmater.2c00326.
- [22] K. Yang, K. Bryce, W. Zhu, D. Zhao, J. Lian, J. Eur. Ceram. Soc. 41 (2021) 2870–2882.
- [23] L. Zhou, F. Li, J.-X. Liu, S.-K. Sun, Y. Liang, G.-J. Zhang, J. Hazard. Mater. 415 (2021) 125596.
- [24] D. Yang, Y. Xia, J. Wen, J. Liang, P. Mu, Z. Wang, Y. Li, Y. Wang, J. Alloys Compd. 693 (2017) 565.
- [25] J. Zhang, J. Lian, A. Fuentes, F. Zhang, M. Lang, F. Lu, R.C. Ewing, Appl. Phys. Lett. 94 (2019) 243110.
- [26] C.A. Taylor, M.K. Patel, J.A. Aguiar, Y. Zhang, M.L. Crespillo, J. Wen, H. Xue, Y. Wang, W.J. Weber, J. Nucl. Mater. 479 (2016) 542–547.
- [27] S. Moll, G. Sattonnay, L. Thomé, J. Jagielski, C. Decorse, P. Simon, I. Monnet, W.J. Weber, Phys. Rev. B 84 (2011) 064115.
- [28] C. Kinsler-Fedon, Q. Zheng, Q. Huang, E.-.S. Choi, J. Yan, H. Zhou, D. Mandrus, V. Keppens, Phys. Rev. Mater. 4 (2020) 104411.
- [29] Y. Zhang, M.L. Crespillo, H. Xue, K. Jin, C.H. Chen, C.L. Fontana, J.T. Graham, W.J. Weber, Nucl. Instruments Methods Phys. Res. Sect. B Beam Interact. Mater. Atoms. 338 (2014) 19–30.
- [30] Y. Zhang, V. Shutthanandan, R. Devanathan, S. Thevuthasan, D.E. McCready, J. Young, G. Balakrishnan, D.M. Paul, W.J. Weber, Nucl. Instruments Methods Phys. Res. Sect. B Beam Interact. Mater. Atoms. 218 (2004) 89–94.
- [31] Y. Zhang, J. Jagielski, I.T. Bae, X. Xiang, L. Thomé, G. Balakrishnan, D.M. Paul, W.J. Weber, Nucl. Instruments Methods Phys. Res. Sect. B Beam Interact. Mater. Atoms. 268 (2010) 3009–3013.
- [32] Y. Zhang, J. Lian, Z. Zhu, W.D. Bennett, L.V. Saraf, J.L. Rausch, C.A. Hendricks, R.C. Ewing, W.J. Weber, J. Nucl. Mater. 389 (2009) 303–310.
- [33] J.F. Ziegler, M.D. Ziegler, J.P. Biersack, Nucl. Instruments Methods Phys. Res. Sect. B Beam Interact. Mater. Atoms. 268 (2010) 1818–1823.
- [34] W.J. Weber, Y. Zhang, Curr. Opin. Solid State Mater. Sci. 23 (2019) 100757.
- [35] B.D. Begg, N.J. Hess, W.J. Weber, R. Devanathan, J.P. Icenhower, S.
- Thevuthasan, B.P. McGrail, J. Nucl. Mater. 288 (2001) 208–216.

 [36] W.J. Weber, Nucl. Instrument. Method. Phys. Res. Sect. B (2000) 98–106, 166–167.
- [37] D. Aidhy, R. Sachan, E. Zarkadoula, O. Pakarinen, M.F. Chisholm, Y. Zhang, W.J. Weber, Sci Rep 5 (2015) 16297.
- [38] R. Sachan, V.R. Cooper, B. Liu, D.S. Aidhy, B.K. Voas, M. Lang, X. Ou, C. Trautmann, Y. Zhang, M.F. Chisholm, W.J. Weber, The J. Phys. Chem. C 121 (2017) 975–981.